



Strong-field ionization of argon: Electron momentum spectra and nondipole effectsNida Haram ^{1,*}, Han Xu,¹ Igor Ivanov,² Dashavir Chetty,¹ Igor Litvinyuk,^{1,†} and R. T. Sang ^{1,‡}¹*Centre for Quantum Dynamics, Griffith University, Brisbane, Queensland 4111, Australia*²*Centre for Relativistic Laser Science, Institute for Basic Science, Gwangju 61005, Republic of Korea*

(Received 28 July 2021; accepted 9 February 2022; published 24 February 2022)

We investigate the influence of relativistic nondipole effects on the photoelectron spectra of argon, particularly in the low-kinetic-energy region (0–1 eV). In our experiment, we use intense, linearly polarized 800-nm laser pulses to ionize Ar from a jet and we record photoelectron energy and momentum distributions using a reaction microscope. Our measurements show that nondipole effects can cause an energy-dependent asymmetry along the laser propagation direction in the photoelectron energy and momentum spectra. Model simulation based on the time-dependent Dirac equation can reproduce our measurement results. Moreover, the electron trajectory analysis based on the classical model reveals that the photoelectrons obtain a negative momentum shift in the laser propagation direction due to the interplay between the Lorentz-force-induced radiation pressure during its free propagation in the continuum and rescattering by the Coulomb potential of the parent ion when it is driven back by the laser field.

DOI: [10.1103/PhysRevA.105.023522](https://doi.org/10.1103/PhysRevA.105.023522)**I. INTRODUCTION**

In strong-field physics, the so-called simple man's three-step model [1] has been proven to be extremely useful for providing quantitative explanations for a wealth of highly nonlinear laser-matter interaction phenomena, such as high-order harmonic generation [2–4], above-threshold ionization (ATI) [5–7], nonsequential double ionization [8–10], frustrated tunneling ionization [11], etc. In this semiclassical model, the laser-matter interaction happens in two main stages. At the first stage, the target atom or molecule is tunnel ionized and a free electron appears in the continuum. At the second stage, the free electron is driven solely by the laser's electric field while the influence of the Coulomb potential is neglected.

The predictions of the simple man's model, however, could not show satisfactory quantitative agreement with the results of high-resolution strong-field experiments. For example, the existence of low-energy structures (LESs), very-low-energy structures, and near-zero-energy structures in the photoelectron energy and momentum spectra obtained as a result of strong-field ionization with low-frequency fields [12–19] arises due to the short-range Coulomb focusing effect, which is an interaction ignored in the simple man's model. Such short-range Coulomb focusing effects can only be observed when the free electron is driven back to its parent ion core with a distance from several tens to 100 a.u. with nearly zero velocity. Since the Coulomb force scales inversely to the distance from the core ($U \sim 1/r$), the long-range Coulomb effect is supposed to be much weaker. The long-range Coulomb effect

has been found to significantly affect the emission angle of the streaked photoelectrons [20] and strongly influence the zero-energy structure of the photoelectron momentum spectrum [21].

The suppression of LESs for the experiments carried out with circularly polarized laser field led to the speculation that their origin might be linked with rescattering [13]. In accordance with the results from circularly polarized laser fields, the time-dependent Schrödinger equation results also suggested that rescattering is involved in the creation of LESs. Initial theoretical investigations [22–24] attributed LESs to be the result of the interplay between forward scattering and the Coulomb focusing effect, which supported the proposition of recollision. Another model suggested that the creation of LESs is linked with the bunching of photoelectrons, which miss the parent ion upon the so-called soft recollisions [25,26]. The insight into these low-energy features is of great importance for photoelectron holography to determine the structural properties of the parent ion [27–29] and to explore the time-resolved tunneling dynamics [20,30].

In this work we investigate the influence of relativistic nondipole effects on the low-energy features of the photoelectron momentum and energy spectra obtained by using a moderately intense linearly polarized near-infrared laser field. These effects become discernible in the form of an offset in the photoelectron momentum distribution along the laser propagation direction [31–36]. The relativistic nondipole effects encompass the short-range Coulomb focusing effect, demonstrating the breakdown of the strong-field approximation and also of the dipole approximation. In the former approximation, the Coulomb interaction of the photoelectron with the parent ion after the ionization is neglected [37,38]. The latter approximation assumes that the electromagnetic field is spatially uniform on the length scale of the electron motion during the laser pulse and the influence of the

*nida.haram@alumni.griffithuni.edu.au

†i.litvinyuk@griffith.edu.au

‡r.sang@griffith.edu.au

magnetic-field component of the laser pulse on the electron motion is negligible compared to that of the electric-field component [39,40]. The breakdown of these approximations gives rise to the relativistic nondipole effects that induce non-negligible momentum transfer to the photoelectrons, which ultimately modifies the low-energy features of the photoelectron momentum and energy spectra [41,42].

We present high-resolution, low-energy photoelectron momentum and energy spectra for the single ionization of Ar by few-cycle, linearly polarized laser pulses (800 nm, 6 fs, 0.8 PW/cm^2) in an exceptionally clean vacuum chamber. The photoelectrons with low kinetic energy demonstrate a tilted cusp structure in the transverse electron momentum distribution (TEM), where transverse momentum refers to the photoelectron momentum perpendicular to the laser polarization plane. This cusp structure is not symmetric about $p_y = 0$ because of the relativistic nondipole effect, where p_y is the transverse momentum along the laser propagation direction. To measure the cusp tilting, we calculate the longitudinal momentum P_{\parallel} dependent asymmetry for the photoelectron momentum along the laser propagation direction, where longitudinal momentum ($P_{\parallel} = p_z$) refers to the photoelectron momentum along laser polarization plane. We show that the strong kinetic energy dependence of the asymmetry is caused by the ionization phase and thus by the trajectory of the tunneled electron. Moreover, for slow photoelectrons, with their kinetic energy close to zero, the propagation trajectory in the continuum allows these electrons to experience strong Coulomb focusing. The experimental results are supported by a truly relativistic *ab initio* model based on the three-dimensional (3D) time-dependent Dirac equation (TDDE) [34].

II. EXPERIMENTAL SYSTEM

The experiment was performed with a commercially available Ti:sapphire laser system in combination with a reaction microscope (REMI). The laser system delivered linearly polarized few-cycle pulses in the near infrared (central wavelength of 800 nm) at a repetition rate of 1 kHz. The inherent ellipticity of the laser pulses was eliminated by a quarter waveplate (QWP). The pulse duration in the reaction zone was controlled by compensating the chirp using a pair of fused silica wedges. The laser beam was tightly focused in the reaction zone inside the ultrahigh vacuum chamber (10^{-10} mbar) by a silver-coated spherical mirror with a focal length of 75 mm. The laser intensity was controlled by using pellicle beam splitters and was chosen such that only single ionization of Ar remains dominant. The laser beam along the y axis was crossed by the supersonic gas jet along the x axis at the laser focus from where the resulting ions and electrons travel along the z axis or time of flight (TOF) axis to their respective detectors of the REMI (see Fig. 1). A half waveplate (HWP) was used to rotate the polarization axis of the laser pulses to the TOF axis of the REMI. The laser intensity in the reaction zone was determined precisely by the recoil-ion momentum imaging method within 10% confidence interval [43,44]. To guarantee the reliability of our data, the laser intensity was constantly monitored during the experiment with intensity fluctuations less than 5%.

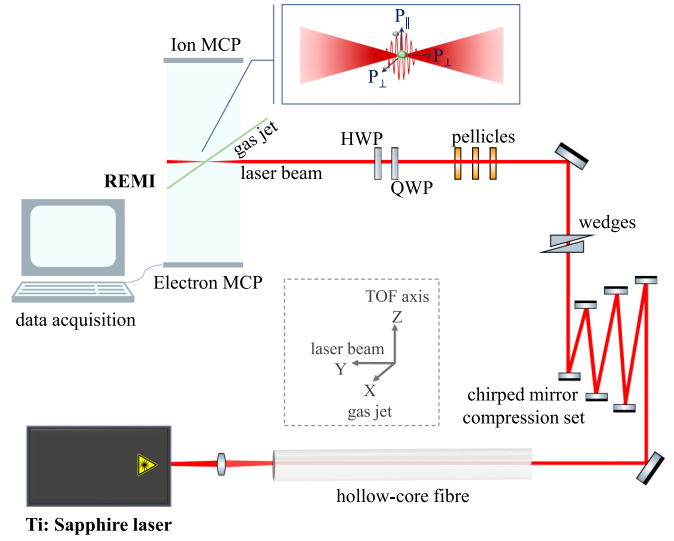


FIG. 1. Experimental setup used to explore the influence of relativistic nondipole effects on the low-energy features of the photoelectron momentum and kinetic energy spectra.

The complete final-state momentum and energy distributions of both electrons and ions were recorded by the REMI [45] with a controlled well-defined momentum resolution. To reduce the electron counts from the background gas, an ion or electron coincidence filter was employed, which selects the Ar^+ and electron pair with a nearly zero-momentum sum. Moreover, the space charge effects were avoided by carefully adjusting the laser intensity and the number density of the supersonic gas jet in the reaction zone such that the empty ionization events (zero ion or electron counts) are dominating (greater than 50%). A very low electric field (55 V/cm) was applied parallel to the TOF axis and laser polarization but perpendicular to the laser beam and supersonic gas jet direction, which guides the low-energy electrons and ions towards two time- and position-sensitive microchannel plate (MCP) and delay line detectors. A homogeneous weak magnetic field (1.95 G) was applied to confine the transverse motion of the electrons to ensure that the electrons with energies less than 30 eV reach the detector. These low values of electric and magnetic field improved the resolution of the REMI such that we were able to observe the low-energy features with high resolution and clarity. Measurements were taken at an intensity of 0.8 PW/cm^2 , which was chosen so as to reduce the space charge effect and avoid depletion of Ar^+ by double ionization.

III. THEORETICAL MODEL BASED ON THE 3D TDDE

To solve the TDDE we follow the procedure described in [34,46–48], which we briefly recapitulate here. Atomic units with $\hbar = 1$, $e = 1$, $m = 1$, and $c \approx 137.036$ (here e and m are the charge and mass of the electron, respectively, and c is the speed of light) are used in the formulas below.

We solve the TDDE for the Ar atom in the field of a laser pulse described by the vector potential $A_z(t - y/c)$ (the pulse is linearly polarized in the z direction and propagates in the y

direction),

$$i \frac{\partial \Psi(\mathbf{r}, t)}{\partial t} = \hat{H} \Psi(\mathbf{r}, t), \quad (1)$$

where $\Psi(\mathbf{r}, t)$ is a four-component wave function (bispinor) and \hat{H} is the Hamiltonian operator

$$\hat{H} = \hat{H}_{\text{atom}} + \hat{H}_{\text{int}}, \quad (2)$$

where

$$\hat{H}_{\text{atom}} = c\boldsymbol{\alpha} \cdot \hat{\mathbf{p}} + c^2(\beta - I) + IV(r) \quad (3)$$

and

$$\hat{H}_{\text{int}} = c\boldsymbol{\alpha} \cdot \mathbf{A}(t, y). \quad (4)$$

The vector potential $A_z(t - y/c)$ in Eq. (4) is defined by

$$\mathbf{A}(t, y) = -\hat{\mathbf{e}}_z \frac{E_0}{\omega} T(\zeta) \sin^2\left(\frac{\pi\zeta}{T_1}\right) \sin(\omega\zeta), \quad (5)$$

where $\zeta = t - y/c$, $T(\zeta)$ is a window function such that $T(\zeta) = 1$ for $\zeta \in (0, T_1)$ and zero outside this interval, $T_1 = 6T$ is the total pulse duration, with $T = 2\pi/\omega$ an optical cycle corresponding to the base frequency $\omega = 0.057$ a.u., and E_0 is the peak field strength of the laser pulse. We use the Dirac basis for the $\boldsymbol{\alpha}$ matrices $\boldsymbol{\alpha} = \begin{pmatrix} 0 & \boldsymbol{\sigma} \\ \boldsymbol{\sigma} & 0 \end{pmatrix}$, $\beta = \begin{pmatrix} I & 0 \\ 0 & -I \end{pmatrix}$, and $I = \begin{pmatrix} I & 0 \\ 0 & I \end{pmatrix}$, where $\boldsymbol{\sigma}$ are Pauli matrices and $\mathbf{0}$ and I are 2×2 null and identity matrices, respectively. We subtracted from the field-free atomic Hamiltonian (3) the rest mass term Ic^2 so that we operate in a more familiar energy scale commonly used in nonrelativistic atomic physics calculations.

The Ar atom is described in the single-active-electron (SAE) approximation. We use for $V(r)$ in Eq. (3) the model potential given in [49]. The solution is represented as a series in basis bispinors

$$\Psi(\mathbf{r}, t) = \sum_{l=j\pm 1/2}^{J_{\text{max}}} \sum_{M=-j}^j \Psi_{j l M}(\mathbf{r}, t), \quad (6)$$

where each basis bispinor is

$$\Psi_{j l M}(\mathbf{r}, t) = \begin{pmatrix} g_{j l M}(r, t) \Omega_{j l M}(\mathbf{n}) \\ f_{j l M}(r, t) \Omega_{j' l' M}(\mathbf{n}) \end{pmatrix} \quad (7)$$

and two-component spherical spinors are defined as

$$\Omega_{j l M}(\mathbf{n}) = \begin{pmatrix} C_{l, M-(1/2)(1/2)(1/2)}^{j M} Y_{l, M-1/2}(\mathbf{n}) \\ C_{l, M+(1/2)(1/2)(-1/2)}^{j M} Y_{l, M+1/2}(\mathbf{n}) \end{pmatrix},$$

where $C_{lm(1/2)\mu}^{jM}$ are the Clebsch-Gordan coefficients, $Y_{lm}(\mathbf{n})$ are the spherical harmonics, and $\mathbf{n} = \mathbf{r}/r$. The parameters l and l' in Eq. (6) must satisfy the relation $l + l' = 2j$. To take into account the nondipole effects due to the spatial dependence of the laser fields, the vector potential in Eq. (4) is expanded in a series of spherical harmonics at every step of the integration procedure.

The radial functions $g_{j l M}(r, t)$ and $f_{j l M}(r, t)$ in Eq. (7) and the Hamiltonian operator \hat{H} are discretized on the grid with the step size $\delta r = 0.05$ a.u. in a box of size $R_{\text{max}} = 2000$ a.u. The maximum value of the parameter j in Eq. (6), chosen to ensure convergence of the bispinor expansion, is $J_{\text{max}} = 100\frac{1}{2}$.

To avoid the nonphysical reflection of parts of the ionized wave packet at the boundaries of the box, we use a complex absorbing potential method, adding a pure imaginary potential term to the Hamiltonian with support concentrated near the boundary [50].

Substituting the expansion (6) in the TDDE (1) and performing some cumbersome but straightforward manipulations using well-known properties of spherical spinors [51], we obtain a set of coupled differential equations for the discretized radial functions $g_{j l M}(r, t)$ and $f_{j l M}(r, t)$ in Eq. (7), which, with the suitable mapping of $g_{j l M}(r_n, t)$ and $f_{j l M}(r_n, t)$ to the components of \mathbf{a}_k , $k = 1, \dots, N$, of a vector \mathbf{a} , can be cast in the form of a system of ordinary differential equations (ODEs)

$$i\dot{\mathbf{a}}(t) = \mathbf{B}(t) \cdot \mathbf{a}(t), \quad (8)$$

where the matrix \mathbf{B} is a Hamiltonian matrix in this basis.

To determine energies of the bound states of the field-free Hamiltonian, we look for the stationary solution of Eq. (8) reduced to a proper symmetry subspace, obtained in the case of a zero external electric field. To actually find such solutions we impose boundary conditions $g_{j l M}(R) = 0$ and $f_{j l M}(R) = 0$ at some point R far from the atom (we use $R = 100$ a.u. in actual calculations) and solve the corresponding eigenvalue problem. The energy eigenvalue for the ground state $3p_{1/2}$ we obtain as a result of this procedure is -0.6025 a.u. We note that use of the SAE approximation does not allow us to take into account spin states of the ionic core. The ionic core's effect on the electron is described in this approach by a single function $V(r)$, which represents the ionic core potential. This however is not a severe limitation for the purposes of the present work. The reason for this is the different magnitude of the nondipole relativistic effects in which we are interested in the present work and the relativistic effects responsible for the appearance of the fine-structure splitting in the atom. The nondipole effects which we are interested in are ultimately due to the nonzero value of the photon momentum or, if we prefer a purely classical picture, due to the appearance of the term y/c in the expression $A_z(t - y/c)$ for the vector potential in Eq. (5). Retaining such terms means that we take into account effects of the order of c^{-1} . On the other hand, the spin-orbit relativistic effects, responsible for the fine-structure splitting of the ionic core, are of the order of c^{-2} . More specifically, the magnitude of these effects scales approximately as $Z^4 \alpha^2$ [52], where Z and $\alpha = e^2/\hbar c$ are the nuclear charge and the fine-structure constant, respectively [52]. These effects are therefore weak for the Ar atom with its relatively low nuclear charge.

For the actual solution of the system of ODEs (8) we write the short-time propagator, driving the solution from t_m to $t_{m+1} = t_m + \Delta$, in the Crank-Nicolson form [53]

$$\mathbf{a}(t_{m+1}) = \frac{\mathbf{I} - \frac{\Delta}{2} \mathbf{B}(t_m + \frac{\Delta}{2})}{\mathbf{I} + \frac{\Delta}{2} \mathbf{B}(t_m + \frac{\Delta}{2})} \cdot \mathbf{a}(t_m). \quad (9)$$

The most time-consuming part in computations of this expression is inversion of the matrix in Eq. (9). This inversion can be efficiently done using a generalization of the well-known matrix iteration method [54], which we described in detail in [46].

Hamiltonian matrix $\mathbf{B}(t_m)$ can be represented as a sum $\mathbf{B}(t) = \mathbf{B}_{\text{atom}} + \mathbf{B}_{\text{int}}(t)$ of the atomic Hamiltonian matrix \mathbf{B}_{atom} and atom-field interaction matrix $\mathbf{B}_{\text{int}}(t)$. For a suitably chosen mapping of $g_{jlm}(r_n, t)$ and $f_{jlm}(r_n, t)$ to components of \mathbf{a} , the matrix \mathbf{B}_{atom} is banded (pentadiagonal). Using the Neumann expansion for the denominator in Eq. (9), we obtain

$$(\mathbf{P} + \hat{\mathbf{Q}})^{-1} = \mathbf{P}^{-1} - \mathbf{P}^{-1}\mathbf{Q}\mathbf{P}^{-1} + \mathbf{P}^{-1}\mathbf{Q}\mathbf{P}^{-1}\mathbf{Q}\mathbf{P}^{-1} - \dots, \quad (10)$$

with $\mathbf{P} = \mathbf{I} + \frac{\Delta}{2}\mathbf{B}_{\text{atom}}$ and $\mathbf{Q} = \frac{\Delta}{2}\mathbf{B}_{\text{int}}(t)$, and using the fact that banded matrix \mathbf{P} can be inverted with little computational cost, we can efficiently compute the matrix inverse prescribed in (9). In practical calculation we retain 20 terms of the Neumann expansion (10) and use the time step Δ in the range (0.005, 0.05) a.u. depending on the field strength.

Differential ionization probabilities are calculated as $P(\mu, \mathbf{p}) = |a(\mu, \mathbf{p})|^2$, where $a(\mu, \mathbf{p})$ are the ionization amplitudes (here μ is, i.e., spin direction in the electron's rest frame, and \mathbf{p} asymptotic electron momentum). The amplitudes are obtained by projecting the solution of the TDDE after the end of the pulse on the set of ingoing relativistic scattering states $\Psi_{\mu, \mathbf{p}}^-(\mathbf{r})$ of the Ar atom calculated numerically using the model potential $V(r)$ in Eq. (3). As we are not able to resolve different electron spin states in the experiment, we sum our results for the probability distributions over electron polarization states.

IV. RESULTS AND DISCUSSION

The photoelectron momentum perpendicular to the laser polarization plane, also known as transverse momentum, carries information about the recollision event caused by Coulomb focusing of the photoelectrons [1, 15, 55–58] without being disturbed by the momentum transfer from the laser field. Therefore, the TEMD is considered as the most suitable spectrum to explore the influence of relativistic nondipole effects on the low-energy features. In addition, the dependence of transverse momentum on the kinetic energy of photoelectrons provides more insight into the underlying physics.

The P_{\parallel} - P_{\perp} resolved 2D photoelectron spectra recorded in our experiment from the strong-field ionization of Ar at an intensity of 0.8 PW/cm² has sufficiently high resolution to resolve the low-energy features. They are revealed as a superposition of multiple symmetric patterns about the polarization axis. In Fig. 2 we can see that the higher-energy region of the spectrum contains a series of intercycle features in the form of ATI rings, whereas intracycle fanlike stripes emerging radially outward in the range $-0.3 < p_{\parallel} < 0.3$ can be seen in the low-energy regions. However, since these features are known to be sensitive to the laser intensity, wavelength, and number of cycles in the laser pulse [59–61], we observe a difference in the details of these features for the experiment and simulation (see Fig. 2). In addition, the focal volume effects, which are not taken into account in the simulation, may also be responsible for the differences observed in the experiment and simulation.

A. Momentum or kinetic energy dependence

The influence of relativistic nondipole effects on the low-energy photoelectrons can be seen in the plot of

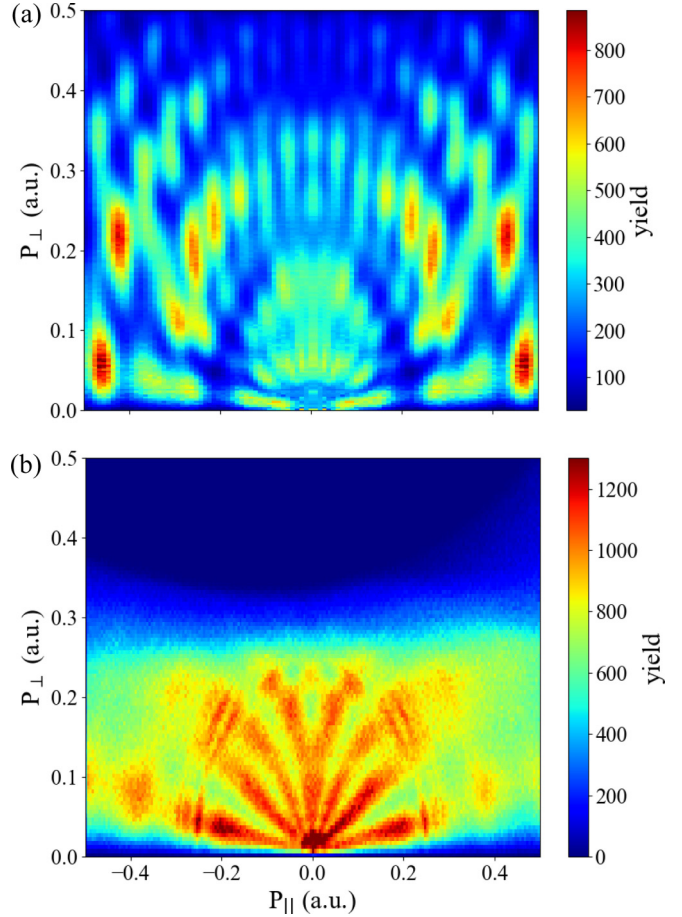


FIG. 2. Longitudinal momentum distribution, i.e., along the laser polarization ($P_{\parallel} = p_z$), vs transverse electron momentum distribution ($P_{\perp} = \sqrt{p_x^2 + p_y^2}$) resulting from the strong-field ionization of Ar using few-cycle pulses (6 fs, 800 nm) at 0.8 PW/cm², representing the intercycle and intracycle interference features: (a) theoretical simulation based on the 3D TDDE and (b) measurement results.

transverse momentum p_y along the laser propagation direction vs photoelectron kinetic energy, showing the tilting for very-low-energy photoelectrons (0–0.5 eV). This tilt is absent for the transverse momentum p_x perpendicular to the laser propagation direction (see Fig. 3).

The photoelectrons with low kinetic energy can experience strong Coulomb focusing. As the low-energy photoelectrons typically get ionized at local maxima or minima of the driving laser waveform and return to the parent ion in one optical cycle, they stay longer around the ion and experience stronger Coulomb attraction. The interaction between the Coulomb focusing and relativistic nondipole effects leads to the spectral narrowing of the low-energy TEMD with the peak shift in the negative direction. However, the high-energy TEMD gets broadened with a forward peak shift. This energy-dependent offset can be used as a self-referencing technique for the detection and analysis of the relativistic nondipole effect, without relying on the autoionization of Rydberg state molecules to calibrate the transverse momentum offset [31, 32].

At an intensity of 0.8 PW/cm², it was already expected and has been already reported that the photoelectrons show a

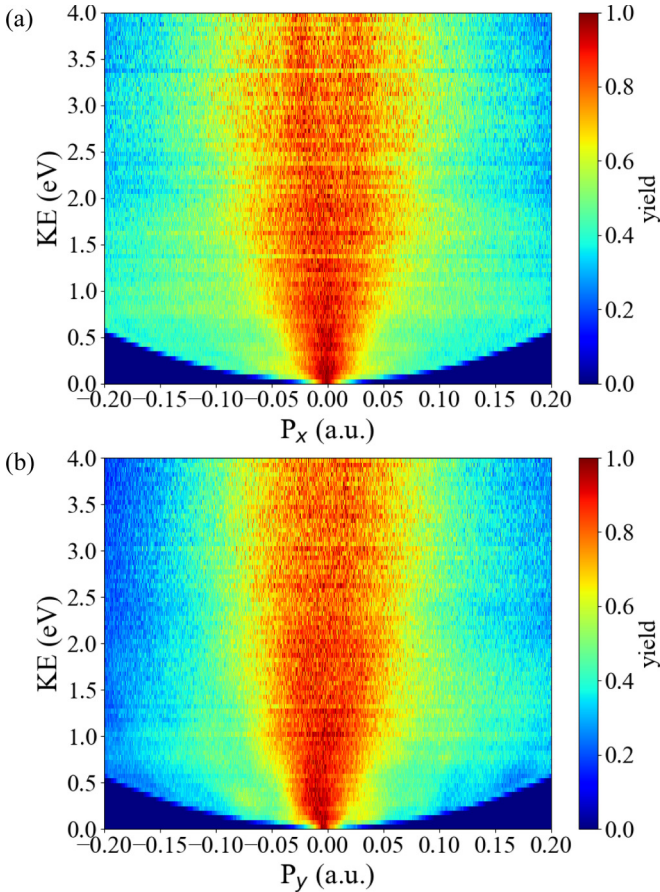


FIG. 3. Energy-resolved transverse electron momentum spectrum of Ar at 0.8 PW/cm² using 800-nm, 6-fs laser pulses. (a) Low-energy electrons for transverse momentum along the laser propagation direction p_y experience a tilt in the negative direction and then in the positive direction with increasing kinetic energy. (b) There is no tilting in the low-energy region for the transverse momentum perpendicular to the laser propagation direction p_x , but a spread can be observed at higher kinetic energy.

negative peak shift. As can be seen in the results from our previous work (Fig. 4), which compares the experimental data obtained in the intensity range 0.6–3.0 PW/cm² with the 3D TDDE simulation results in the intensity range 0.5–7.0 PW/cm², the peak corresponding to the very-low-energy electrons continues shifting in the negative direction with increasing intensity [34]. This peak shift was determined with reference to the data obtained at the lowest intensity.

A comparison of the tilt as observed in the simulated TEMD along the laser propagation direction at two different intensities 0.3 and 0.8 PW/cm² is presented in Fig. 5. It is evident from the figure that the momentum distribution is symmetric about zero momentum, i.e., $p_y = 0$ at low intensity [Fig. 5(a)]. A very small shift in Fig. 5(a) seems to appear in the positive direction, which can be considered insignificant due to the limited resolution. However, at a higher intensity, not only are the very-low-energy electrons shifted in the negative direction, but also the tilt of the photoelectron momentum distribution is quite obvious [Fig. 5(b)].

Furthermore, we compare the measurement and simulated normalized spectra of the transverse electron momentum

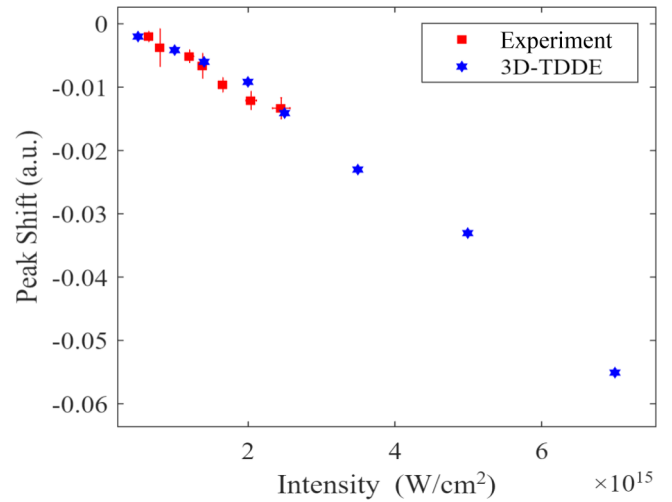


FIG. 4. With increasing intensity in the range 0.5–7.0 PW/cm², the relative peak shift of the TEMD obtained as a result of strong-field ionization of Ar using few-cycle laser pulses (6 fs, 800 nm) increases in the negative direction.

along the laser propagation direction p_y vs longitudinal momentum $P_{||}$ at an intensity of 0.8 PW/cm², as shown in Figs. 6(a) and 6(b). To qualitatively assess the tilting of peaks presented in Figs. 6(a) and 6(b), we plot the asymmetries of these 2D momentum distributions in Figs. 6(c) and 6(d), where the asymmetry parameter is defined as

$$A = (N_R - N_L)/(N_R + N_L), \quad (11)$$

where N_R and N_L correspond to the yield on the right- and left-hand sides of the momentum distribution with reference to $p_y = 0$. These results show overall good agreement between experiment and theory in the whole momentum range, other than the features of the simulation results which are absent in the measurement due to the limitations of experimental conditions.

Figure 7 presents the measured kinetic-energy (KE)-resolved transverse electron momentum spectrum at 0.8 PW/cm² and the corresponding KE-dependent peak shift for the low-energy (0–1 eV) photoelectrons. The analysis is based on determining the peak position of the transverse momenta p_y along the laser propagation direction integrated

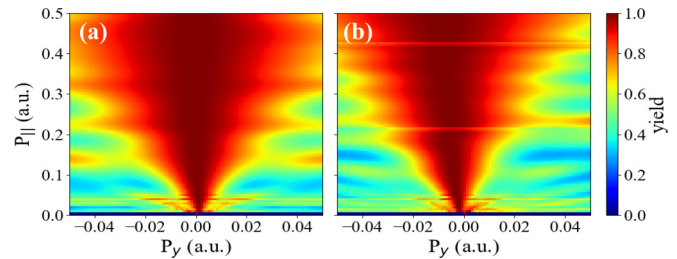


FIG. 5. Simulation results based on the 3D TDDE using similar laser parameters as used in the experiment: normalized spectra of the transverse electron momentum along the laser propagation direction p_y vs longitudinal momentum $P_{||}$ obtained by the strong-field ionization of Ar using few-cycle laser pulses (6 fs, 800 nm) at (a) low (0.3 PW/cm²) and (b) high (0.8 PW/cm²) intensities.

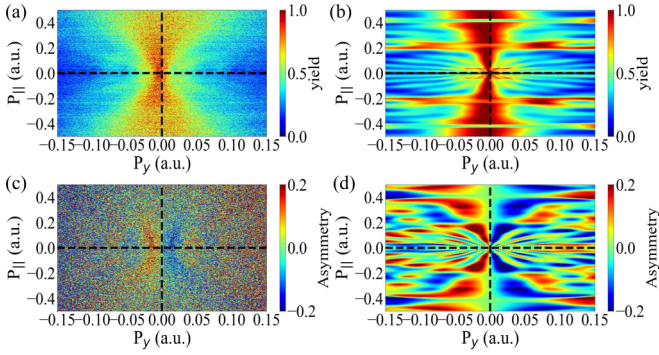


FIG. 6. Normalized spectra of transverse momentum along the laser propagation direction p_y vs longitudinal momentum P_{\parallel} at a high intensity of 0.8 PW/cm^2 : (a) measurement results and (b) simulation results. Also shown is the asymmetry of the (c) measurement and (d) simulated results for the strong-field ionization of Ar using 800-nm, 6-fs laser pulses.

over the energy range of 0.1 eV as a function of photoelectron energy by employing the same fitting procedure as used in [34]. To highlight the features of interest, we zoom in on the transverse momentum along the laser propagation direction p_y in a narrow range of 0.15 a.u. and extract the peak position of the transverse momentum p_y integrated over the energy range of 0.1 eV. The peak shift is determined by the asymmetry in the cusp of the TEMD. For this purpose, the function $V(p_y) \equiv \ln W(p_y)$ is analyzed in a narrow range of transverse momenta $|p_y| \leq 0.15$ a.u., where $W(p_y)$ is the ionization rate. The experimental data are fitted with the function $V(p_y) = B + A|p_y - \beta|^\alpha$ by performing a series of least-squares fits, where A , B , α , and β are the fitting parameters with β accountable for the peak shift $\langle p_y \rangle$.

It is clear that the zero-energy or close-to-zero-energy electrons show a negative peak shift which keeps on increasing in the negative direction for the photoelectrons having energy lower than 0.2 eV. The cause of this negative shift is the strong Coulomb focusing effect for the electrons having close-to-zero energy. The very-low-energy photoelectrons in the range

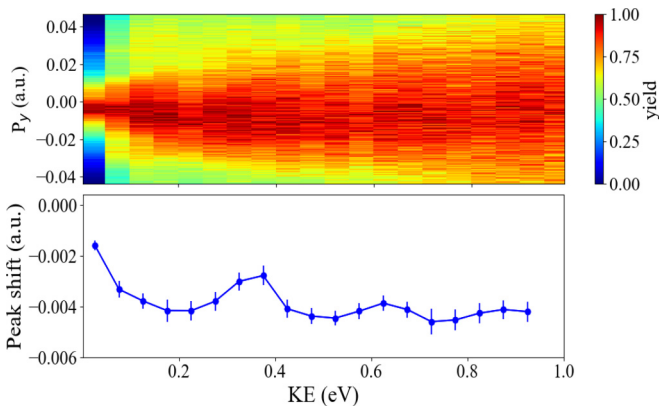


FIG. 7. Kinetic-energy-resolved transverse electron momentum spectrum along the laser propagation direction P_y based on the measurement results of strong-field ionization of Ar using few-cycle laser pulses (6 fs, 800 nm) at 0.8 PW/cm^2 and the corresponding KE resolved peak shift.

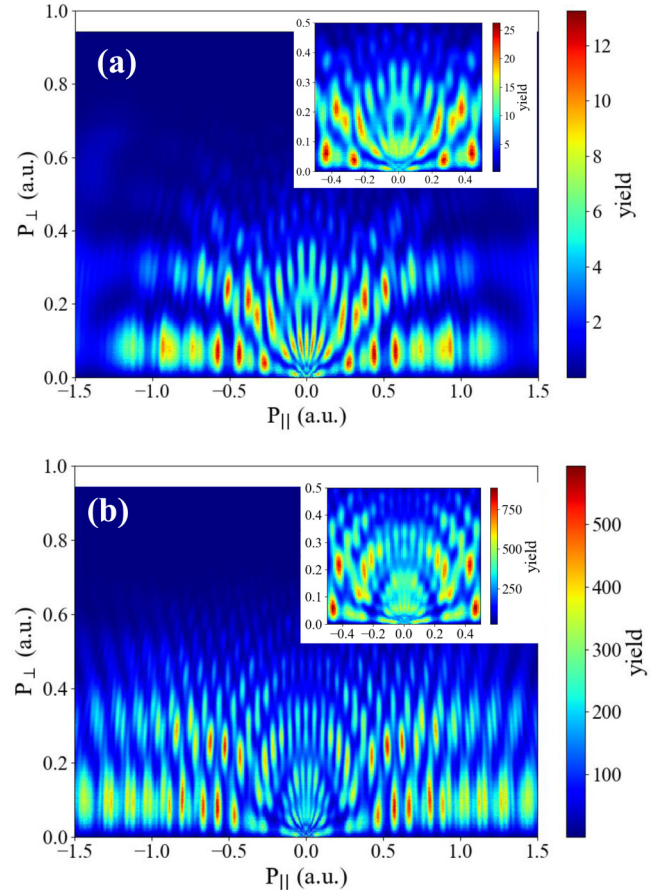


FIG. 8. CEP-averaged photoelectron momentum distributions of strong-field ionization of Ar using few-cycle laser pulses (6 fs, 800 nm) at (a) low intensity (0.3 PW/cm^2) and (b) high intensity (0.8 PW/cm^2).

0.2–0.37 eV then experience a forward shift, perhaps as a result of the radiation pressure. The shift pattern continues to oscillate from a negative-positive-negative shift in this small energy range (0–1 eV). The change in sign of this peak shift for the low-energy electrons (less than 1 eV) may also be dependent on the trajectories they are following.

B. Carrier-envelope-phase dependence

1. Carrier-envelope-phase-averaged momentum distributions

The simulated carrier-envelope-phase (CEP)-averaged photoelectron momentum distributions based on the 3D TDDE at 0.3 and 0.8 PW/cm^2 are shown in Figs. 8(a) and 8(b). In general, these spectra exhibit a number of features, mainly consisting of intercycle and intracycle interferences. Intercycle interferences cause the momentum distribution to evolve in concentric ATI rings centered at zero momentum and are formed as a result of the superposition of electron trajectories corresponding to a complex release time during multiple optical cycles. These rings are insensitive to the Coulomb potential and their yield depends upon the direction of photoelectron emission [59,62]. Regular carpetlike features are created by the interference of ATI rings that are separated by a number of cycles [57,63]. Intracycle interferences lead

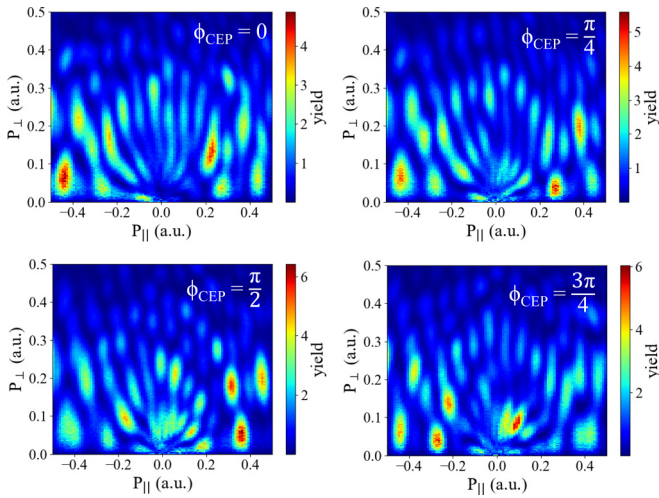


FIG. 9. CEP-dependent photoelectron momentum distributions at low intensity (0.3 PW/cm²).

to the formation of fanlike stripes caused by the interference of electron trajectories within one optical cycle. These include the direct photoelectron trajectories and the trajectories corresponding to those electrons which are deflected by the Coulomb potential without experiencing any hard recollisions [64]. The intracycle interferences are also responsible for the coherent superposition of distinct states known as Freeman resonances. These resonant features are formed as a result of a range of intensities attributed to the focal volume below the peak intensity [65]. The pattern of these fanlike features exhibits a strong dependence on the wavelength since it influences the states to be populated with a particular angular quantum number l [60]. The fine holographic features beside the main features emerge from the intracycle interferences between the direct photoelectron trajectories and the trajectories that correspond to hard recollisions [66].

It has been established that the features in the photoelectron momentum distributions are sensitive to the laser wavelength and intensity [60,61]. Since we are comparing the momentum distributions at two quite different intensities, the number of ATI rings and fanlike stripes as well as their patterns are found to be significantly different (see Fig. 8). Considering these momentum distributions are CEP averaged, the features are found to be symmetric about $p_{\parallel} = 0$.

2. CEP-dependent momentum distributions

The CEP has a profound effect on the photoelectron momentum distributions. The spectra obtained at two different intensities show quite unique features for each CEP as shown in Figs. 9 and 10.

The features are significantly different for different CEP values, i.e., not alike or symmetric, since a specific CEP value may enhance the population of only a particular resonant feature. However, as reported earlier in our previous paper, the effect of the CEP on the nondipole effects is not resolvable within experimental uncertainty [34]. In order to explore these effects, the peak shift of the TEMD along the laser propagation direction was extracted for the sine and cosine pulses, which turned out to be the much smaller than

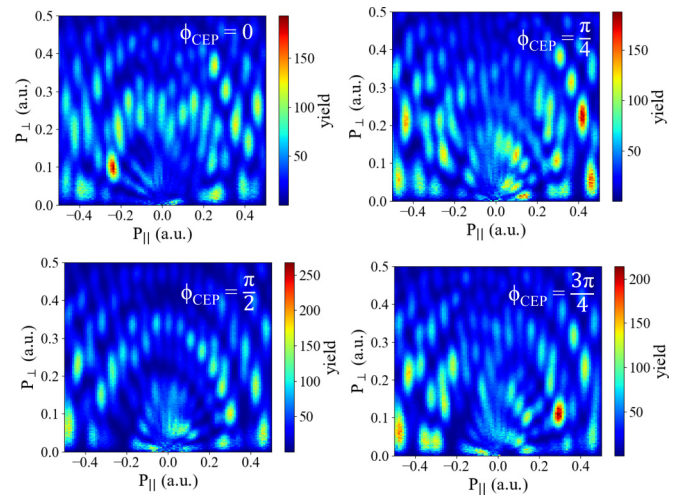


FIG. 10. CEP-dependent photoelectron momentum distributions obtained by the strong-field ionization of Ar using few-cycle laser pulses (6 fs, 800 nm) at high intensity (0.8 PW/cm²).

the experimental uncertainty. Further investigation based on the simulation results at 0.3 and 0.8 PW/cm² supports the previous results showing that for different CEP values the peak shift is extremely small, especially at lower intensity (see Fig. 11).

V. CLASSICAL ANALYSIS

To investigate the role of photoelectron trajectories on the relativistic nondipole effects, a simple physical picture based on a modified three-step model is presented. In the first step, the electron is ionized close to the peak of the laser electric field. In the next step, the photoelectron is accelerated by the driving laser field along its polarization axis and follows its oscillatory motion with a constant drift motion given by the laser field at the tunnel exit. Due to this drift momentum, which the photoelectron possesses when the laser pulse is

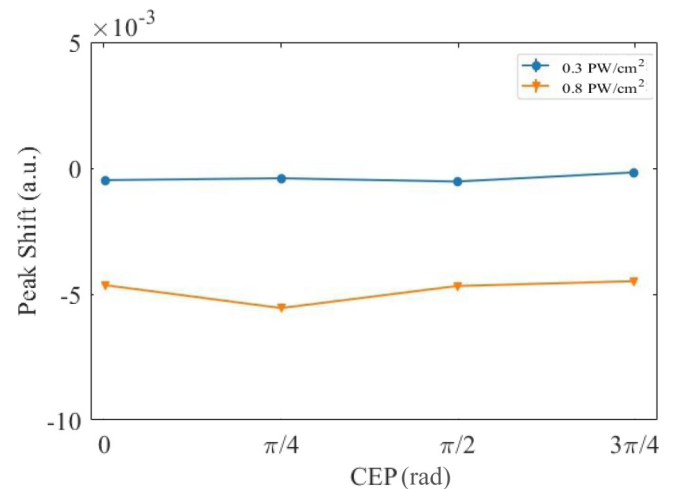


FIG. 11. CEP-dependent peak shift of the TEMD along the laser propagation direction P_y obtained by the strong-field ionization of Ar using few-cycle laser pulses (6 fs, 800 nm) at 0.3 and 0.8 PW/cm².

over, the photoelectron gets detected at the detector. However, perpendicular to the polarization axis, the photoelectron is pushed along its propagation axis with a constant velocity due to the Lorentz force. In the third step, the photoelectron obtains a negative transverse momentum when it revisits and gets elastically scattered by the Coulomb potential of the parent ion, which is similar to the Rutherford scattering process. The drift momentum gained in the second step is responsible for the particular trajectories that allow the low-energy rescattering and cause the photoelectron to be strongly focused. Thus, the negative photoelectron momentum shift is sensitive to the photoelectron trajectory and it happens within one optical cycle.

Classical electron trajectory model

The validity of this modified three-step model can be confirmed by performing a pure classical electron trajectory simulation for different ionization times. Experimentally, it can be confirmed by using a CEP locked few-cycle pulse or two-color laser field to break the top-bottom symmetry, which is beyond the scope of the present work. In this way, the photoelectron trajectory and its momentum shift along the laser propagation direction are expected to be different for $P_{\parallel} > 0$ and $P_{\parallel} < 0$.

Here we have performed a full classical electron trajectory simulation. The pump laser is propagating along the y axis and its electric-field component is linearly polarized along the z axis,

$$\begin{pmatrix} E_x \\ E_y \\ E_z \end{pmatrix} = \begin{pmatrix} 0 \\ 0 \\ E_0 \sin^2\left(\frac{\pi(t-\frac{y}{c})}{\tau_0}\right) \cos\left[\omega\left(t - \frac{y}{c}\right) + \phi_0\right] \end{pmatrix}, \quad (12)$$

where E_0 is the peak electric-field strength (0.06 a.u.), τ_0 is the pulse duration (five optical cycles), ω is the pump laser carrier frequency, ϕ_0 is the CEP, and c is the speed of light in vacuum. The magnetic-field component of the pump laser is linearly polarized along the x axis,

$$\begin{pmatrix} B_x \\ B_y \\ B_z \end{pmatrix} = \begin{pmatrix} -E_z \\ 0 \\ 0 \end{pmatrix}. \quad (13)$$

The dynamics of the electron in the presence of the pump electric and magnetic fields, as well as the Coulomb potential force from the ion, is given by

$$\begin{pmatrix} F_x \\ F_y \\ F_z \end{pmatrix} = \begin{pmatrix} -\frac{dU(r)}{dr} \frac{x}{r} \\ \frac{B_x}{c} v_z - \frac{dU(r)}{dr} \frac{y}{r} \\ -eE_z - \frac{B_x}{c} v_y - \frac{dU(r)}{dr} \frac{z}{r} \end{pmatrix}, \quad (14)$$

where $U(r) = -1/\sqrt{r^2 + s}$ is a soft-core Coulomb potential with $s = 0.1$ a.u.; $r = \sqrt{x^2 + y^2 + z^2}$ is the distance between the electron and ion; and

v_x , v_y , and v_z are the three electron velocity components. Given the initial conditions, including electron tunneling time t_0 and exit site $(0, 0, z_0)$, and assuming zero initial velocity after tunneling ionization, the final 3D momentum and position of the free electron can be calculated by solving the Newton function (14), where an integration time of seven

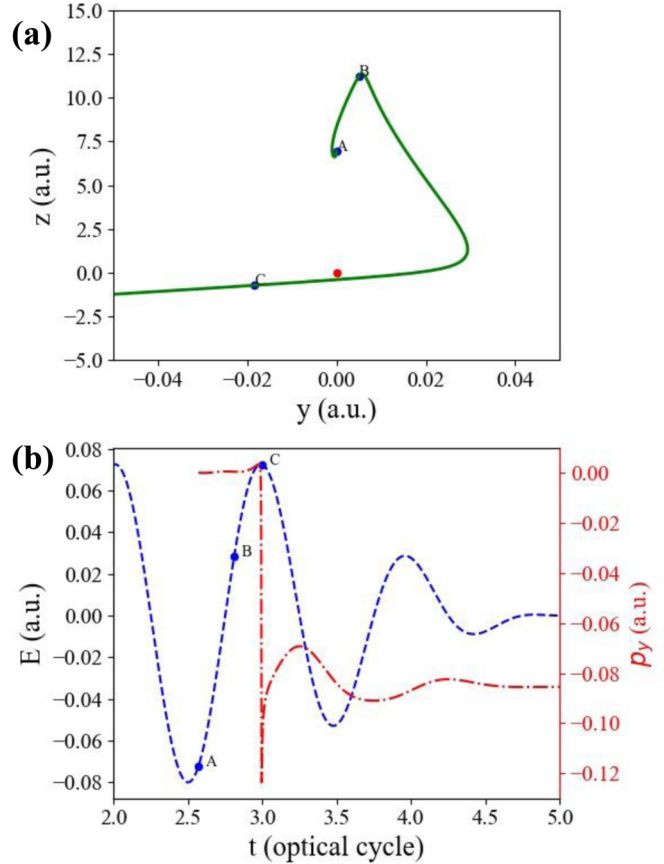


FIG. 12. (a) Calculated typical electron trajectory with negative momentum along the laser propagation direction, where the initial exit position $z_0 = 6.97$ a.u., the initial velocity $v_{z_0} = -0.184$ a.u., and $t_0 = 2.57$ o.p. is used in the classical simulation. (b) Time evolution of the driving electric field (blue dashed curve) and time-dependent electron momentum P_y . The points A, B, and C in (a) indicate the electron position when $t = 2.57$ o.p. [point A in (b)], $t = 2.81$ o.p. [point B in (b)], and $t = 2.996$ o.p. [point C in (b)], respectively.

optical periods (o.p.) is used. By scanning the tunneling time t_0 and exit site position z_0 , we found the negative peak shift of the TEMD that corresponds to the electrons having tunneling time at around the local peaks of the driving electric field and the exit site around $z_0 = 6.97$ a.u.

Figure 12 shows a typical electron trajectory with negative momentum shift along the y axis, where the electron is ionized at $t_0 = 2.57$ o.p. (electric field is peaked at 2.5 o.p.), the exit site is $(x_0 = 0, y_0 = 0, z_0 = 6.97$ a.u.), and the exit velocity is $(v_{x_0} = 0, v_{y_0} = 0, v_{z_0} = -0.184$ a.u.). Within half optical cycle, the electron is driven away from the parent ion and reaches the largest ion or electron distance at $t = 2.81$ o.p. After that, the electron is driven back towards the ion and gains a positive spatial displacement along the laser propagation direction (y axis) due to the radiation pressure produced by the laser field. At $t = 3.0$, the electron is rescattered by the parent ion and gains a negative momentum which is opposite to the laser propagation direction. An electron trajectory with positive momentum along the y axis is possible for electrons which have not experienced rescattering. Figure 13

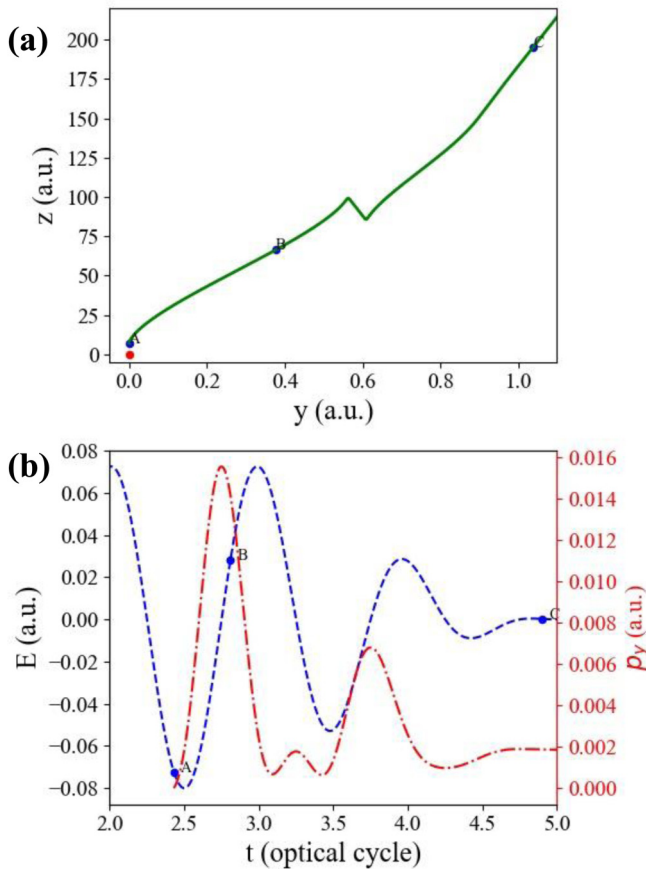


FIG. 13. Same as Fig. 12 but with ionization time set as $t_0 = 2.43$ o.p., the exit site as $(x_0 = 0, y_0 = 0, z_0 = 6.97$ a.u.), and the exit velocity as $(v_{x_0} = 0, v_{y_0} = 0, v_{z_0} = 0.184$ a.u.). The points A, B, and C in (a) indicate the electron position when $t = 2.43$ o.p. [point A in (b)], $t = 2.81$ o.p. [point B in (b)], and $t = 4.9$ o.p. [point C in (b)], respectively.

shows a typical electron trajectory with positive momentum shift; the electron is no longer driven back to its parent

ion and the electron can gain positive momentum along the y axis.

VI. CONCLUSION AND OUTLOOK

We have investigated how the low-energy features of the photoelectron momentum and energy spectra are impacted by the relativistic nondipole effects for an ultrashort linearly polarized near-infrared laser field. The measured and simulated photoelectron momentum spectra for Ar show very interesting sharp features in the form of ATI rings and Freeman resonances due to the intercycle and intracycle resonances. Further investigations of the energy-resolved relativistic nondipole effects revealed an asymmetry or tilt in both momentum and energy spectra. It was shown that the central peak shift for the low-energy electrons is always in the negative direction with reference to the laser propagation direction. However, the high-energy electrons that also form the wings of the TEMD contribute towards the positive shift. Moreover, this peak shift was found to be oscillating between the negative and positive directions, which can be ascribed to specific electron trajectories as explored by classical analysis based on a modified three-step model. The influence of the CEP on the relativistic nondipole effects has also been investigated, showing that it has a very small effect on the peak shift of the TEMD such that it is difficult to resolve within experimental uncertainty.

ACKNOWLEDGMENTS

This research was supported by the Australian Research Council Discovery Project No. DP190101145. We also acknowledge support from the Institute for Basic Science, Gwangju, Republic of Korea, under Grant No. IBS-R012-D1. N.H. and D.C. were supported by Griffith University International Postgraduate Research Scholarship. H.X. was supported by an ARC Discovery Early Career Researcher Award No. DE130101628.

N.H. and H.X. contributed equally to this work.

- [1] P. B. Corkum, *Phys. Rev. Lett.* **71**, 1994 (1993).
- [2] A. McPherson, G. Gibson, H. Jara, U. Johann, T. S. Luk, I. A. McIntyre, K. Boyer, and C. K. Rhodes, *J. Opt. Soc. Am. B* **4**, 595 (1987).
- [3] M. Ferray, A. L'Huillier, X. F. Li, L. A. Lompre, G. Mainfray, and C. Manus, *J. Phys. B* **21**, L31 (1988).
- [4] M. W. Walser, C. H. Keitel, A. Scrinzi, and T. Brabec, *Phys. Rev. Lett.* **85**, 5082 (2000).
- [5] P. B. Corkum, N. H. Burnett, and F. Brunel, *Phys. Rev. Lett.* **62**, 1259 (1989).
- [6] J. Eberly, J. Javanainen, and K. Rzażewski, *Phys. Rep.* **204**, 331 (1991).
- [7] D. B. Milošević, G. G. Paulus, D. Bauer, and W. Becker, *J. Phys. B* **39**, R203 (2006).
- [8] D. N. Fittinghoff, P. R. Bolton, B. Chang, and K. C. Kulander, *Phys. Rev. Lett.* **69**, 2642 (1992).
- [9] B. Walker, B. Sheehy, L. F. DiMauro, P. Agostini, K. J. Schafer, and K. C. Kulander, *Phys. Rev. Lett.* **73**, 1227 (1994).
- [10] B. Feuerstein, R. Moshhammer, D. Fischer, A. Dorn, C. D. Schröter, J. Deipenwisch, J. R. Crespo Lopez-Urrutia, C. Höhr, P. Neumayer, J. Ullrich, H. Rottke, C. Trump, M. Wittmann, G. Korn, and W. Sandner, *Phys. Rev. Lett.* **87**, 043003 (2001).
- [11] T. Nubbemeyer, K. Gorling, A. Saenz, U. Eichmann, and W. Sandner, *Phys. Rev. Lett.* **101**, 233001 (2008).
- [12] C. I. Blaga, J. Xu, A. D. DiChiara, E. Sistrunk, K. Zhang, P. Agostini, T. A. Miller, L. F. DiMauro, and C. D. Lin, *Nature (London)* **483**, 194 (2012).
- [13] F. H. M. Faisal, *Nat. Phys.* **5**, 319 (2009).
- [14] C. Y. Wu, Y. D. Yang, Y. Q. Liu, Q. H. Gong, M. Wu, X. Liu, X. L. Hao, W. D. Li, X. T. He, and J. Chen, *Phys. Rev. Lett.* **109**, 043001 (2012).
- [15] W. Quan, Z. Lin, M. Wu, H. Kang, H. Liu, X. Liu, J. Chen, J. Liu, X. T. He, S. G. Chen, H. Xiong, L. Guo, H. Xu, Y. Fu, Y. Cheng, and Z. Z. Xu, *Phys. Rev. Lett.* **103**, 093001 (2009).

- [16] J. Dura, N. Camus, A. Thai, A. Britz, M. Hemmer, M. Baudisch, A. Senftleben, C. D. Schröter, J. Ullrich, R. Moshhammer, and J. Biegert, *Sci. Rep.* **3**, 2675 (2013).
- [17] M. G. Pullen, J. Dura, B. Wolter, M. Baudisch, M. Hemmer, N. Camus, A. Senftleben, C. D. Schroeter, R. Moshhammer, J. Ullrich, and J. Biegert, *J. Phys. B* **47**, 204010 (2014).
- [18] B. Wolter, C. Lemell, M. Baudisch, M. G. Pullen, X.-M. Tong, M. Hemmer, A. Senftleben, C. D. Schröter, J. Ullrich, R. Moshhammer, J. Biegert, and J. Burgdörfer, *Phys. Rev. A* **90**, 063424 (2014).
- [19] B. Wolter, M. G. Pullen, M. Baudisch, M. Sclafani, M. Hemmer, A. Senftleben, C. D. Schröter, J. Ullrich, R. Moshhammer, and J. Biegert, *Phys. Rev. X* **5**, 021034 (2015).
- [20] B. Willenberg, J. Maurer, B. W. Mayer, and U. Keller, *Nat. Commun.* **10**, 5548 (2019).
- [21] W. Quan, X. Hao, Y. Chen, S. Yu, S. Xu, Y. Wang, R. Sun, X. Lai, C. Wu, Q. H. Gong, X. He, X. Liu, and J. Chen, *Sci. Rep.* **6**, 27108 (2016).
- [22] T.-M. Yan, S. V. Popruzhenko, M. J. J. Vrakking, and D. Bauer, *Phys. Rev. Lett.* **105**, 253002 (2010).
- [23] C. Liu and K. Z. Hatsagortsyan, *Phys. Rev. Lett.* **105**, 113003 (2010).
- [24] C. F. d. M. Faria and A. Maxwell, *Rep. Prog. Phys.* **83**, 034401 (2020).
- [25] A. Kästner, U. Saalman, and J. M. Rost, *Phys. Rev. Lett.* **108**, 033201 (2012).
- [26] A. Kästner, U. Saalman, and J. M. Rost, *J. Phys. B* **45**, 074011 (2012).
- [27] M. Meckel, D. Comtois, D. Zeidler, A. Staudté, D. Pavičić, H. C. Bandulet, H. Pépin, J. C. Kieffer, R. Dörner, D. M. Villeneuve, and P. B. Corkum, *Science* **320**, 1478 (2008).
- [28] X.-B. Bian and A. D. Bandrauk, *Phys. Rev. Lett.* **108**, 263003 (2012).
- [29] M. Meckel, A. Staudté, S. Patchkovskii, D. M. Villeneuve, P. B. Corkum, R. Dörner, and M. Spanner, *Nat. Phys.* **10**, 594 (2014).
- [30] G. Porat, G. Alon, S. Rozen, O. Pedatzur, M. Krüger, D. Azoury, A. Natan, G. Orenstein, B. D. Bruner, M. J. J. Vrakking, and N. Dudovich, *Nat. Commun.* **9**, 2805 (2018).
- [31] C. T. L. Smeenk, L. Arissian, B. Zhou, A. Mysyrowicz, D. M. Villeneuve, A. Staudte, and P. B. Corkum, *Phys. Rev. Lett.* **106**, 193002 (2011).
- [32] A. Ludwig, J. Maurer, B. W. Mayer, C. R. Phillips, L. Gallmann, and U. Keller, *Phys. Rev. Lett.* **113**, 243001 (2014).
- [33] I. Ivanov, A. Kheifets, J. Calvert, S. Goodall, X. Wang, H. Xu, A. Palmer, D. Kielpinski, I. Litvinyuk, and R. Sang, *Sci. Rep.* **6**, 19002 (2016).
- [34] N. Haram, I. Ivanov, H. Xu, K. T. Kim, A. Atia-tul-Noor, U. S. Sainadh, R. D. Glover, D. Chetty, I. V. Litvinyuk, and R. T. Sang, *Phys. Rev. Lett.* **123**, 093201 (2019).
- [35] A. Hartung, S. Eckart, S. Brennecke, J. Rist, D. Trabert, K. Fehre, M. Richter, H. San, S. Zeller, K. Henrichs, G. Kastirke, J. Hoehl, A. Kalinin, M. S. Schöffler, T. Jahnke, L. P. H. Schmidt, M. Lein, M. Kunitski, and R. Dörner, *Nat. Phys.* **15**, 1222 (2019).
- [36] A. Hartung, S. Brennecke, K. Lin, D. Trabert, K. Fehre, J. Rist, M. S. Schöffler, T. Jahnke, L. P. H. Schmidt, M. Kunitski, M. Lein, R. Dörner, and S. Eckart, *Phys. Rev. Lett.* **126**, 053202 (2021).
- [37] F. Marco, *Phys. Rev. A* **45**, 43 (1992).
- [38] M. Y. Ivanov, M. Spanner, and O. Smirnova, *J. Mod. Opt.* **52**, 165 (2005).
- [39] H. R. Reiss, *Prog. Quantum Electron.* **16**, 1 (1992).
- [40] N. Haram, R. T. Sang, and I. V. Litvinyuk, *J. Phys. B* **53**, 154005 (2020).
- [41] H. R. Reiss, *Opt. Express* **2**, 261 (1998).
- [42] H. R. Reiss, *Phys. Rev. A* **87**, 033421 (2013).
- [43] A. S. Alnaser, X. M. Tong, T. Osipov, S. Voss, C. M. Maharjan, B. Shan, Z. Chang, and C. L. Cocke, *Phys. Rev. A* **70**, 023413 (2004).
- [44] C. Smeenk, J. Z. Salvail, L. Arissian, P. B. Corkum, C. T. Hebeisen, and A. Staudté, *Opt. Express* **19**, 9336 (2011).
- [45] J. Ullrich, R. Moshhammer, A. Dorn, R. Dörner, L. P. H. Schmidt, and H. Schmidt-Böcking, *Rep. Prog. Phys.* **66**, 1463 (2003).
- [46] I. A. Ivanov, *Phys. Rev. A* **91**, 043410 (2015).
- [47] I. A. Ivanov, *Phys. Rev. A* **96**, 013419 (2017).
- [48] I. A. Ivanov and Y. K. Ho, *Phys. Rev. A* **69**, 023407 (2004).
- [49] A. Sarsa, F. J. Gálvez, and E. Buendia, *At. Data Nucl. Data Tables* **88**, 163 (2004).
- [50] L. A. A. Nikolopoulos, *Elements of Photoionization Quantum Dynamics Methods* (Morgan & Claypool, San Rafael, 2019), pp. 2053–2571.
- [51] E. M. Lifshitz and V. B. Berestetskii, *Quantum Electrodynamics* (Pergamon, New York, 1982).
- [52] I. I. Sobelman, *Introduction to the Theory of Atomic Spectra* (Pergamon, New York, 1972).
- [53] A. Goldberg, H. M. Schey, and J. L. Schwartz, *Am. J. Phys.* **35**, 177 (1967).
- [54] M. Nurhuda and F. H. M. Faisal, *Phys. Rev. A* **60**, 3125 (1999).
- [55] T. Brabec, M. Y. Ivanov, and P. B. Corkum, *Phys. Rev. A* **54**, R2551 (1996).
- [56] C. Blaga, F. Catoire, P. Colosimo, G. Paulus, H. Muller, P. Agostini, and L. DiMauro, *Nat. Phys.* **5**, 335 (2009).
- [57] P. A. Korneev, S. V. Popruzhenko, S. P. Goreslavski, T.-M. Yan, D. Bauer, W. Becker, M. Kübel, M. F. Kling, C. Rödel, M. Wünsche, and G. G. Paulus, *Phys. Rev. Lett.* **108**, 223601 (2012).
- [58] H. Liu, Y. Liu, L. Fu, G. Xin, D. Ye, J. Liu, X. T. He, Y. Yang, X. Liu, Y. Deng, C. Wu, and Q. Gong, *Phys. Rev. Lett.* **109**, 093001 (2012).
- [59] D. G. Arbó, K. L. Ishikawa, E. Persson, and J. Burgdörfer, *Nucl. Instrum. Methods Phys. Res. Sect. B* **279**, 24 (2012).
- [60] T. Marchenko, H. G. Muller, K. J. Schafer, and M. J. J. Vrakking, *J. Phys. B* **43**, 185001 (2010).
- [61] T. Marchenko, Y. Huismans, K. J. Schafer, and M. J. J. Vrakking, *Phys. Rev. A* **84**, 053427 (2011).
- [62] D. G. Arbó, S. Yoshida, E. Persson, K. I. Dimitriou, and J. Burgdörfer, *Phys. Rev. Lett.* **96**, 143003 (2006).
- [63] P. A. Korneev, S. V. Popruzhenko, S. P. Goreslavski, W. Becker, G. G. Paulus, B. Fetić, and D. B. Milošević, *New J. Phys.* **14**, 055019 (2012).
- [64] X.-Y. Lai, C. Poli, H. Schomerus, and C. F. d. M. Faria, *Phys. Rev. A* **92**, 043407 (2015).
- [65] R. R. Freeman, P. H. Bucksbaum, H. Milchberg, S. Darack, D. Schumacher, and M. E. Geusic, *Phys. Rev. Lett.* **59**, 1092 (1987).
- [66] A. S. Maxwell, A. Al-Jawahiry, T. Das, and C. F. d. M. Faria, *Phys. Rev. A* **96**, 023420 (2017).